

Machine Learning Product State Distributions from Initial Reactant States for a Reactive Atom-Diatom Collision System

Julian Arnold,^{1,2} Juan Carlos San Vicente Veliz,² Debasish Koner,^{2,3} Narendra Singh,⁴ Raymond J. Bemish,⁵ and Markus Meuwly^{2, a)}

¹⁾*Department of Physics, University of Basel, Klingelbergstrasse 80, CH-4056 Basel, Switzerland*

²⁾*Department of Chemistry, University of Basel, Klingelbergstrasse 80, CH-4056 Basel, Switzerland*

³⁾*Department of Chemistry, Indian Institute of Science Education and Research (IISER) Tirupati, Karakambadi Road, Mangalam, Tirupati 517507, Andhra Pradesh, India*

⁴⁾*Department of Mechanical Engineering, Stanford University, Stanford, CA 94305, USA*

⁵⁾*Air Force Research Laboratory, Space Vehicles Directorate, Kirtland AFB, New Mexico 87117, USA*

(Dated: 8 November 2021)

A machine learned (ML) model for predicting product state distributions from specific initial states (state-to-distribution or STD) for reactive atom-diatom collisions is presented and quantitatively tested for the $\text{N}(^4\text{S}) + \text{O}_2(\text{X}^3\Sigma_g^-) \rightarrow \text{NO}(\text{X}^2\Pi) + \text{O}(^3\text{P})$ reaction. The reference data set for training the neural network (NN) consists of final state distributions determined from explicit quasi-classical trajectory (QCT) simulations for ~ 2000 initial conditions. Overall, the prediction accuracy as quantified by the root-mean-squared difference (~ 0.003) and the R^2 (~ 0.99) between the reference QCT and predictions of the STD model is high for the test set and off-grid state specific initial conditions and for initial conditions drawn from reactant state distributions characterized by translational, rotational and vibrational temperatures. Compared with a more coarse grained distribution-to-distribution (DTD) model evaluated on the same initial state distributions, the STD model shows comparable performance with the additional benefit of the state resolution in the reactant preparation. Starting from specific initial states also leads to a more diverse range of final state distributions which requires a more expressive neural network to be used compared with DTD. Direct comparison between explicit QCT simulations, the STD model, and the widely used Larsen-Borgnakke (LB) model shows that the STD model is quantitative whereas the LB model is qualitative at best for rotational distributions $P(j')$ and fails for vibrational distributions $P(v')$. As such the STD model can be well-suited for simulating nonequilibrium high-speed flows, e.g., using the direct simulation Monte Carlo method.

^{a)}Electronic mail: m.meuwly@unibas.ch

I. INTRODUCTION

Predicting the outcomes of chemical reactions is one of the essential tasks for efficient material design, engineering, or reaction planning.¹ Understanding chemical reactions at a molecular level can also shed light on the mechanisms underlying chemical transformations. However, the exhaustive characterization of reactions at the microscopic (i.e. state-to-state or STS) level quickly becomes computationally intractable using conventional approaches due to the rapid growth of the underlying state space.^{2,3} As an example, even for a reactive atom+diatom system ($A+BC\rightarrow AB+C$) the number of internal states for diatoms AB and BC is $\sim 10^4$ which leads to $\sim 10^8$ state-to-state cross sections $\sigma_{v,j\rightarrow v',j'}(E_{\text{trans}})$ between initial (v, j) and final (v', j') rovibrational states at a given relative translational energy E_{trans} .³ The estimated number of classical trajectories required for converged STS cross sections is $\sim \mathcal{O}(10^{13})$ assuming that 10^5 classical trajectories are sufficient for one converged cross section. For reactive diatom+diatom systems this number increases to $\sim \mathcal{O}(10^{20})$ which is currently unfeasible.⁴

Machine learning (ML) methods are well suited for such tasks as they are designed for large data sets and generalize well towards unseen input data.^{1,5} In particular, neural network (NN)-based models have successfully been used to predict the STS cross sections of reactive atom-diatom collision systems.³ These models were trained on data obtained from explicit quasi-classical trajectory (QCT) simulations. Similarly, NN-based models were constructed at the distribution-to-distribution (DTD) level.⁶ For a given set of distributions of initial states of reactants $(P(E_{\text{trans}}), P(v), P(j))$, a DTD model aims at predicting the relative translational energy distribution $P(E'_{\text{trans}})$, together with the vibrational $P(v')$ and rotational $P(j')$ state distributions of the product. Compared with a STS model, state specificity is lost in a DTD model as it follows how a distribution of initial reactant states is processed through interactions on a potential energy surface (PES), but does not keep track of the interrelations between individual initial and final states. This information loss makes DTD models computationally cheaper compared with STS models.

Motivated by these findings, the present work explores the possibility to conceive an intermediate model between the STS and DTD models which retains state specific information

for the reactants. In the following it is demonstrated how a NN-based state-to-distribution (STD) model for a reactive atom+diatom system can be developed. The STD model is shown to predict product state distributions $P(E'_{\text{trans}})$, $P(v')$, and $P(j')$ given a specific initial reactant state (E_{trans}, v, j) . The necessary reference data to train such a NN-based STD model was obtained from explicit quasi-classical trajectory (QCT) simulations for the $\text{N}(^4\text{S})+\text{O}_2(\text{X}^3\Sigma_g^-) \rightarrow \text{NO}(\text{X}^2\Pi) + \text{O}(^3\text{P})$ collision system as a proxy. As such, an STD model may be constructed from a STS model through coarse graining, i.e. by integration of the final states. Similarly, a DTD model can be obtained from an STD model by further coarse graining of the state-specific initial conditions. Note that such a coarse graining by means of integration does, however, incur a computational overhead. Moreover, the increase in information content going from a DTD model to a STD model, and finally to a STS model, also comes at an increased number of trainable parameters and, hence, increased computational cost both in training and evaluation of the model. Therefore, it is crucial to choose the appropriate model resolution for a given task. Finally, it is shown that the STD model realizes a favourable trade-off between computational cost and accuracy, i.e., information content. In particular, the STD model provides information at an appropriate resolution to be utilized as input for methods such as Direct Simulation Monte Carlo (DSMC)⁷ or computational fluid dynamics (CFD) simulations.⁸

This work is structured as follows. First, the methods including the data generation based on quasi-classical trajectory simulations, as well as the neural network architecture and its training are described. Next, the ability of the STD model to predict product state distributions from unseen, specific initial states of the reactant is assessed. Then, the differences between DTD and STD models at predicting product state distributions from initial state distributions is discussed. Finally, the performance of the STD model is compared with the widely used Larsen-Borgnakke⁹ for simulations of nonequilibrium, high-speed flows, and then conclusions are drawn.

II. METHODS

A. Quasi-Classical Trajectory Simulations

Explicit QCT calculations for the $\text{N} + \text{O}_2 \rightarrow \text{NO} + \text{O}$ reaction were carried out following previous work.^{10–14} Specifically, the reactive channel for NO formation ($\text{N}(^4\text{S}) + \text{O}_2(\text{X}^3\Sigma_g^-) \rightarrow \text{NO}(\text{X}^2\Pi) + \text{O}(^3\text{P})$) was considered here. For this, the $^4\text{A}'$ PES was chosen as NO formation is dominated by contributions from the $^4\text{A}'$ electronic state.¹⁴ Hamilton’s equations of motion were solved in reactant Jacobi coordinates using a fourth-order Runge-Kutta method with a time step of $\Delta t = 0.05$ fs, which guarantees conservation of the total energy and angular momentum.^{13,15}

For generating the training, test, and validation data set for the NN the following *state-specific* initial conditions were used: ($0.5 \leq E_{\text{trans}} \leq 8.0$) eV with $\Delta E_{\text{trans}} = 0.5$ eV; $v = [0, 2, 4, 6, 8, 10, 12, 15, 18, 21, 24, 27, 30, 34, 38]$; and $0 \leq j \leq 225$ with $\Delta j = 15$, resulting in 2184 different states. The impact parameter b was sampled from 0 to $b_{\text{max}} = 12 a_0$ using stratified sampling.^{10,16} Ro-vibrational states of the reactant (O_2) and product diatom (NO) are determined from the semiclassical theory of bound states.¹⁵ First, final vibrational and rotational states were determined as real numbers from the diatomic internal energy and angular momentum, respectively, whereas the translational energy is obtained from the relative velocity of the atom+diatom system. Ro-vibrational quantum numbers are then assigned as the nearest integers (v', j') using the histogram binning method. To conserve total energy, the ro-vibrational energy $E_{v'j'}$ is recomputed from semiclassical quantization^{10,15} using the quantum numbers (v', j') and the final translational energy for the atom+diatom system is adjusted using $E'_{\text{trans}} = E_{\text{tot}} - E_{v'j'}$. Product states were assigned using histogram binning ($0.1 \leq E'_{\text{trans}} \leq 19.8$) eV; $0 \leq v' \leq 47$ with $\Delta v' = 1$; $0 \leq j' \leq 240$ with $\Delta j' = 1$. Out of the 2184 initial reactant states, 7 (with $E_{\text{trans}} = 0.5$ eV) resulted in product state distributions with zero or negligible probability ($\max(P) < 10^{-5}$) which were not considered for the subsequent analysis. Consequently, 2177 initial reactant states together with the corresponding product state distributions obtained by QCT simulations constitute the reference data to train and test NN-based STD models in this work.

To evaluate the trained models, a second set of initial conditions was generated from reactant *state distributions*. For each trajectory they were randomly chosen using standard Monte Carlo methods.^{10,11} The initial relative translational energies E_{trans} were sampled from Maxwell-Boltzmann distributions ($0.0 \leq E_{\text{trans}} \leq 19.8$) eV with $\Delta E_{\text{trans}} = 0.1$ eV. Vibrational (v) and rotational (j) states were sampled from Boltzmann distributions, where $0 \leq v \leq 38$ with $\Delta v = 1$; and $0 \leq j \leq 242$ with $\Delta j = 1$. These distributions are characterized by T_{trans} , T_{vib} , and T_{rot} , respectively.^{10,16} For each set of temperatures $\mathbf{T} = (T_{\text{trans}}, T_{\text{vib}}, T_{\text{rot}})$, 80000 trajectories were run to obtain the product state distributions. First, models were constructed with $T_{\text{rovib}} = T_{\text{rot}} = T_{\text{vib}}$, for which QCT simulations were performed at T_{trans} and T_{rovib} ranging from 5000 K to 20000 K in increments of 250 K. This yielded 3698 sets of reactant states and corresponding product state distributions. Next, for the more general case $T_{\text{rot}} \neq T_{\text{vib}}$, additional QCT simulations were performed for $T_{\text{trans}} = 5000, 10000, 15000, 20000$ K with T_{vib} and T_{rot} each ranging from 5000 K to 20000 K in increments of 1000 K. Combining these additional 960 data sets with the 3698 sets from above leads to a total of 4658 data sets.

B. Data Preparation

An important step in conceiving a ML model is the preparation, representation and featurization of the data. For featurization the following properties were chosen as input to the NN: 1.) E_{trans} , 2.) vibrational quantum number v of the diatomic, 3.) rotational quantum number j of the diatomic, 4.) relative velocity of diatom and atom, 5.) internal energy $E_{v,j}$, of the diatom, 6.) vibrational energy $E_{v,j=0}$, of the diatom, 7.) rotational energy $E_{v=0,j}$, of the diatom, 8.) angular momentum of the diatom, 9-10.) the two turning points at each of the vibrational states of the reactant diatom, and 11.) the vibrational time period of the diatom. These features were already used successfully for the STS model.³

To represent the product state distributions, a grid-based (G-based) approach was used.⁶ In a G-based approach, each product state distribution is characterized by its values at discrete grid points, referred to as ‘‘amplitudes’’ in the following. Figure 1 shows the product state distributions from QCT simulations (solid line) and their G-based representation (open

symbols) for two exemplar reactant states. The G-based representation closely follows the true, underlying data from the QCT simulations. Thus, G-based product state distributions (i.e. amplitudes) are suitable to train the NN and the amplitudes also constitute the output of the trained NN. Calculating the product state amplitudes for all available data sets then allowed to train and test the NN. Subsequently, inter- and extrapolation can be performed to obtain a continuous prediction. This is referred to as the “STD model” in the following.

For the product state distributions it was found to be advantageous to consider the set $(P(E'_{\text{int}}), P(v'), P(j'))$ instead of $(P(E'_{\text{trans}}), P(v'), P(j'))$. Here, $E'_{\text{int}} = E_{\text{tot}} - E'_{\text{trans}}$ is the internal energy after removing the translational energy. Note that $P(E'_{\text{int}})$ and $P(E'_{\text{trans}})$ contain the same information and can be interconverted because the total energy E_{tot} of the system is conserved. However, for representing $P(E'_{\text{int}})$ fewer grid points are required than for representing $P(E'_{\text{trans}})$. This is illustrated in Figure 2, where $P(E'_{\text{trans}})$ and $P(E'_{\text{int}})$

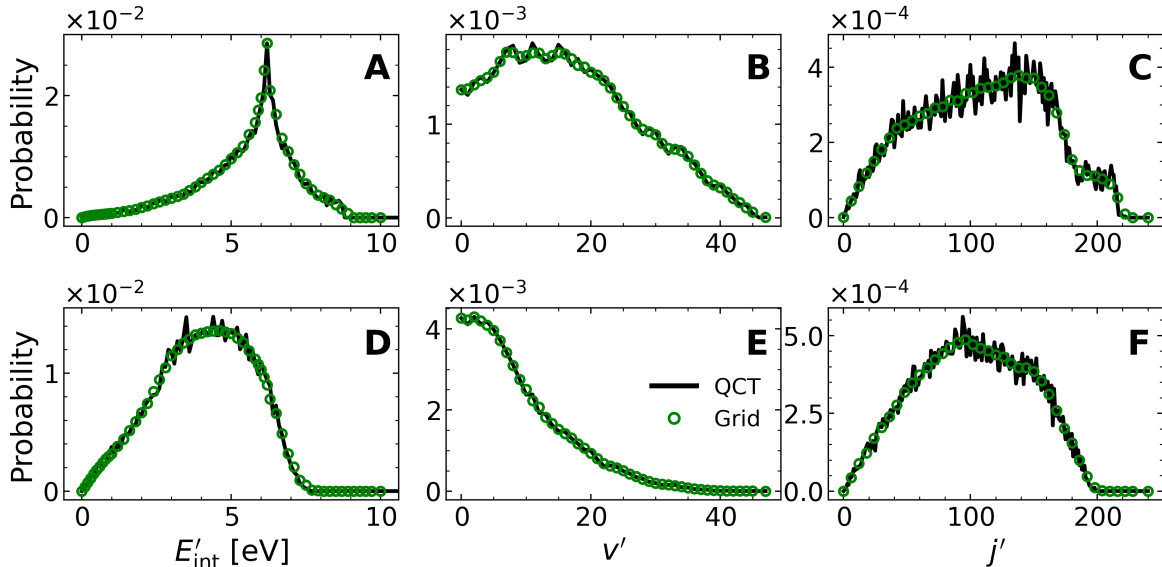


FIG. 1. Product state distributions $P(E'_{\text{int}})$, $P(v')$, and $P(j')$ obtained from QCT simulations (QCT), as well as the corresponding amplitudes that serve as a reference for training and testing the NN-based STD models (Grid). The product state distributions correspond to initial reactant states characterized by: (A to C) ($E_{\text{trans}} = 3.0$ eV, $v = 34$, $j = 0$; $E_{\text{int}} = 4.8$ eV), (D to F) ($E_{\text{trans}} = 5.0$ eV, $v = 6$, $j = 45$; $E_{\text{int}} = 1.5$ eV).

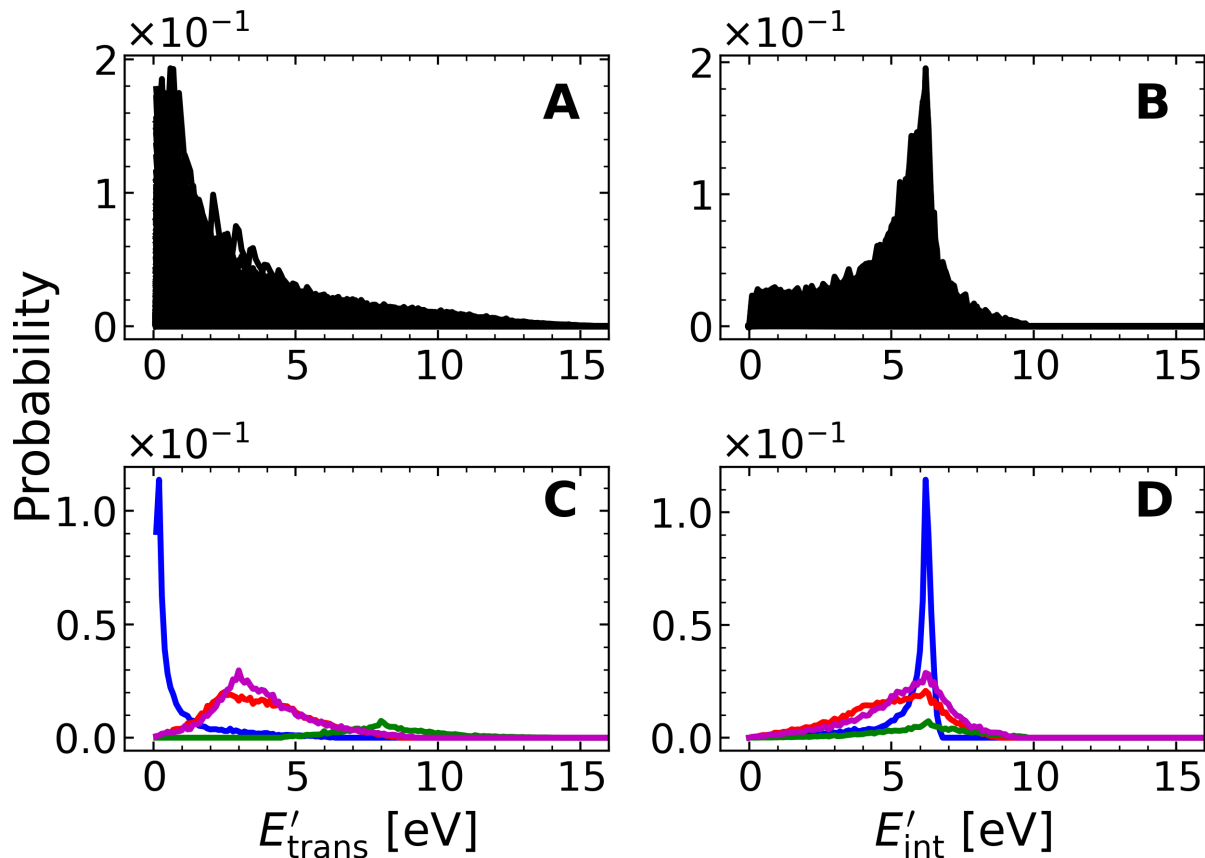


FIG. 2. Distributions $P(E'_{\text{trans}})$ (panel A) and $P(E'_{\text{int}})$ (panel B) obtained from QCT simulations for each of the 2184 initial reactant states considered in this work displayed on top of each other. Panels C and D: a few selected distributions $P(E'_{\text{trans}})$ and $P(E'_{\text{int}})$ to highlight their different shapes that motivate the choice of $P(E'_{\text{int}})$ over $P(E'_{\text{trans}})$.

obtained from explicit QCT simulations for all 2184 initial reactant states used to train and validate in this work are shown. While there are distributions $P(E'_{\text{trans}})$ which are non-zero at $E'_{\text{trans}} > 10$ eV, all $P(E'_{\text{int}})$ are zero for $E'_{\text{int}} > 10$ eV and grid points are only used up to this value.

The location and number of grid points to represent the product state distributions was motivated after inspection of the overall shape of these distributions. In particular, it was observed that a large number of $P(E'_{\text{int}})$ distributions exhibit a sharp peak for $E'_{\text{int}} \sim 6.2$ eV which is the dissociation energy of the product diatom NO (see Figures 1A, 2B and

D).¹⁷ Non-zero contributions to $P(E'_{\text{int}})$ at E'_{int} larger than the dissociation energy of the product diatom NO can be attributed to the presence of quasi-bound states. Additionally, $P(E'_{\text{int}})$ can also increase rapidly for $E'_{\text{int}} < 1.0$ eV. Consequently, the grid for $P(E'_{\text{int}})$ was chosen more densely for $E'_{\text{int}} < 1.0$ eV and $E'_{\text{int}} \sim 6.2$ eV to capture these features ($E'_{\text{int}} = [0.0, 0.1, \dots, 1.0], [1.2, 1.4, \dots, 6.0], [6.1, 6.2, 6.3], [6.5, 6.7, \dots, 9.7, 10.0]$ eV).

A considerable number of the final state vibrational distributions, $P(v')$, show a maximum for $v' \sim 0$ (see Figures 1B and 1E). For higher v' , $P(v')$ typically decays rapidly but in general, the distributions display a variety of shapes. Hence, the corresponding grid was dense ($0 \leq v' \leq 47$ with $\Delta v' = 1$). Final state rotational distributions, $P(j')$, are closer in overall shape to one another compared with $P(E'_{\text{int}})$ or $P(v')$. In particular, $P(j')$ typically does not exhibit sharp features (see Figures 1C and D). Taking this into consideration, the grid for $P(j')$ was equidistant ($0 \leq j' \leq 240$ with $\Delta j' = 6$) and less dense than for the other two final state distributions.

The number of grid points for $(E'_{\text{int}}, v', j')$ was (58, 47, 40), respectively. This is significantly more dense than the DTD model,⁶ for which (16, 16, 12) grid points were used and is attributed to the fact that the distributions considered here are more diverse and exhibit more detail, including sharp features. The shapes of the distributions $P(E'_{\text{int}})$, $P(v')$ or $P(j')$ are generally smooth across the ranges of E'_{int} and quantum numbers v' and j' . They also tend to vary smoothly as the initial state changes. However, when reaction channels open there can be sharp features in the probability distribution, see Figure S1. Because the grids used here are dense, linear interpolation can be used to obtain a continuous NN-based prediction of product state distributions at off-grid points.

Instead of directly sampling the product state distributions $P(x)$ at the grid points x_i to obtain the amplitudes in the G-based representation, local averaging according to

$$\bar{P}(x_i) = \frac{1}{2n+1} \sum_{j=i-n}^{i+n} P(x_j), \quad (1)$$

was performed. Here, the number of neighbouring data points x_j (not necessarily grid points) considered for averaging is $n \in [0, n_{\text{max}}]$. If there are fewer neighbouring data points to the right and/or to the left of grid point x_i when compared with n_{max} , n was chosen as the

maximum number of neighbouring data points available to both sides, otherwise $n = n_{\max}$. Consequently, the first and last data points were assigned unaveraged values. Note, that the value of n_{\max} can differ for each of the 3 degrees of freedom (E'_{int}, v', j'). Additionally, no local averaging was performed for “sharp” peaks and only a reduced amount was applied at nearby points. A maximum was classified as “sharp” if the slopes of the two lines fit to neighbouring data points to the left and right of it exceeded a given threshold, see Section S1 in the SI for details.

C. Neural Network

The NN architecture for the STD model is shown in Figure 3 and is inspired by ResNet.¹⁸ The input and output layers consist of 11 inputs (the 11 features, see above) and $58 + 47 + 40 = 145$ output nodes for the amplitudes characterizing the product state distributions. The main part of the NN consists of 7 residual layers, each of which is again composed of two hidden layers, and two separate hidden layers. The shortcut connections, characteristic for residual layers, help to address the vanishing gradient problem.¹⁸ Hidden layers 1 to 14 are each composed of 11 nodes, whereas hidden layers 14 to 16 are each composed of 44 nodes which leads to a “funnel-like” NN architecture that helps to bridge the gap between the small number of inputs (11) and the large number of outputs ($58 \times 47 \times 40 = 109040$). The NN for the STD model has 3746 trainable parameters compared with ≈ 140 parameters that are used in the DTD model.⁶ The larger number of trainable parameters for STD can be attributed to the larger diversity of product state distributions requiring a denser grid, i.e., a wider output layer. Moreover, the decrease in the number of free model parameters in going from STD to DTD reflects the reduced information content which is the state-specificity on the reactant side.

Before training the NN inputs were standardized via the transformation

$$x'_i = (x_i - \bar{x}_i)/\sigma_i, \tag{2}$$

and the NN outputs are normalized

$$x'_i = x_i/\sigma_i, \tag{3}$$

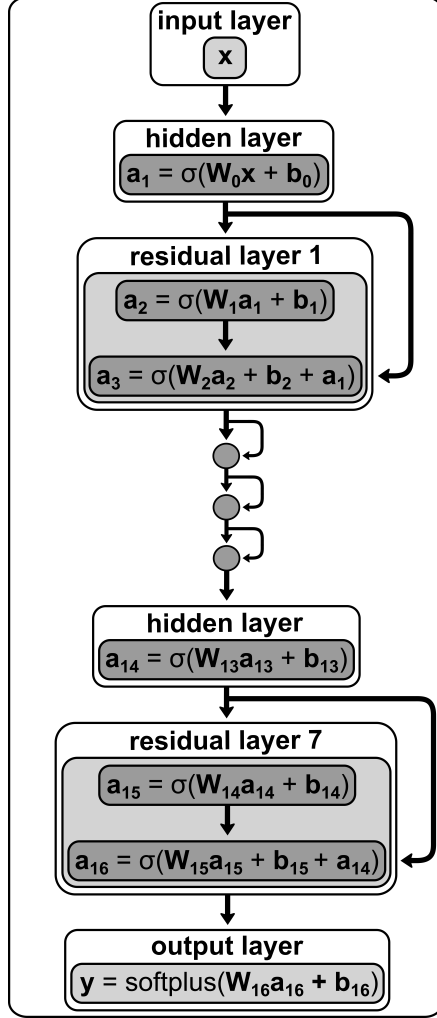


FIG. 3. Schematic for the NN architecture underlying the STD model. The activation vector of each layer is denoted as \mathbf{a}_i , and the input and output vectors are \mathbf{x} and \mathbf{y} . The weight matrix and bias vector for each layer are denoted by \mathbf{W}_i and \mathbf{b}_i , respectively. The activation function of the hidden layers is $\sigma(\mathbf{z})$ and corresponds to a shifted softplus¹⁹ function $\sigma(\mathbf{z}) = \ln(1 + e^{\mathbf{z}}) - \ln(2)$, where $\text{softplus}(\mathbf{z}) = \ln(1 + e^{\mathbf{z}})$.^{20,21} Activation functions act element-wise on vectors.

where x_i denotes the i -th input/output (as specified above), and \bar{x}_i and σ_i are the mean and standard deviation of the distribution of the i -th input/output over the entire training data. Standardization results in distributions of the transformed inputs x'_i over the training data that are characterized by $(\bar{x}'_i = 0, \sigma'_i = 1)$ and allows prediction of high- and low-amplitude data with similar accuracy. Also, standardization generally yields faster convergence of the gradient-based optimization.²¹ The distributions of the transformed outputs x'_i over the training data have $(\bar{x}'_i = \bar{x}_i, \sigma'_i = 1)$ through normalization. This enables the use of a

root-mean-squared deviation (RMSD) loss function

$$\mathcal{L} = \sqrt{\frac{1}{N} \sum_{i=1}^N (y_i - y'_i)^2}. \tag{4}$$

where y_i and y'_i denote the value of the i -th predicted and reference amplitude, respectively. Unnormalized output may drastically differ in amplitude and spread which can lead to poor performance of the RMSD loss. However, this ignores inherent sampling noise arising from potentially unconverged QCT simulations, a point considered explicitly in the following. Using a softplus activation function for the output layer was found to significantly increase the NN prediction accuracy compared in contrast to a scaled hyperbolic tangent. Specifically, using softplus removes unphysical undulations and unphysical negative probabilities which would arise in the predicted product distributions in regions where the corresponding reference distributions are small or zero.

The weights and biases of the NN were initialized according to the Glorot scheme²² and optimized using Adam²³ with an exponentially decaying learning rate. The NN was trained using TensorFlow²⁴ and the set of weights and biases resulting in the smallest loss as evaluated on the validation set were subsequently used for predictions. From the total number of $N_{\text{tot}} = 2177$ data sets, $N_{\text{train}} = 1700$ were randomly selected for training, $N_{\text{valid}} = 400$ were used for validation and $N_{\text{test}} = 77$ were used as the test set.³ All NNs underlying the STD models in this work were trained on a 3.6 GHz Intel Core i7-9700k CPU resulting in training times shorter than 4 minutes.

III. RESULTS

First, the performance of the STD model in predicting product state distributions given specific initial reactant states is discussed. This is done for the test set ($N_{\text{test}} = 77$) and a considerably broader set of initial conditions not covered in training or validation (off-grid). In a next step, the capability of the STD model to predict product state distributions given distributions over initial reactant states is assessed. These include distributions with $T_{\text{trans}} = T_{\text{vib}} = T_{\text{rot}}$, $T_{\text{trans}} \neq T_{\text{vib}} = T_{\text{rot}}$, $T_{\text{trans}} = T_{\text{rot}} \neq T_{\text{vib}}$ as the most relevant case for hypersonics, and $T_{\text{trans}} \neq T_{\text{vib}} \neq T_{\text{rot}}$ as the most general case. The results for $T_{\text{vib}} \neq T_{\text{rot}}$

are also compared with those from the DTD model⁶.

A. Performance for Given Initial States

The performance measures to assess the quality of the STD model considered are $\text{RMSD} = \sqrt{\sum_{i=1}^N \frac{(P_i - O_i)^2}{N}}$ and $R^2 = 1 - \sum_{i=1}^N \frac{(P_i - O_i)^2}{(O_i - \langle O \rangle)^2}$ where P_i is the predicted value i from STD, O_i is the observed (reference) value i from QCT, and $\langle O \rangle$ is the average for a given initial condition and a given degree of freedom. The performance measures are determined for all three degrees of freedom individually and for their entirety. The subscript “LG” refers to evaluating the STD and QCT models only on the locally averaged grid points, whereas the subscript “FG” refers to using all grid points at which QCT data is available (full grid). For this comparison the reference and predicted amplitudes are first normalized with the normalization calculated by numerical integration of the reference QCT distributions. Predictions for STD at off-grid points are obtained through linear interpolation.

| STD model | RMSD _{LG} | R^2_{LG} | RMSD _{FG} | R^2_{FG} |
|-------------------|--------------------|-------------------|--------------------|-------------------|
| overall | 0.0039 | 0.9886 | 0.0033 | 0.9890 |
| E'_{int} | 0.0095 | 0.9915 | 0.0077 | 0.9906 |
| v' | 0.0020 | 0.9885 | 0.0018 | 0.9895 |
| j' | 0.0003 | 0.9860 | 0.0003 | 0.9867 |

TABLE I. Performance measures RMSD and R^2 for the test set ($N_{\text{test}} = 77$). The mean error is calculated separately using the distributions of E'_{int} , v' , or j' and then averaged to obtain an overall performance measure. Subscripts “LG” and “FG” refer to the “local grid” (on which STD is evaluated) and “full grid” (on which the reference QCT results are available).

The performance measures of the STD model on the test set are summarized in Table I. Overall, $\text{RMSD}_{\text{LG}} = 0.0039$ and $R^2_{\text{LG}} = 0.9886$ values confirm that the NN gives highly accurate predictions of the amplitudes on a grid characterizing the product state distributions. The performance is preserved even for the “full grid” (FG). The decreasing performance for predicting $P(E'_{\text{int}})$ compared to $P(v')$ or $P(j')$ (see RMSD and R^2 in Table I) can be

attributed to the fact that $P(E'_{\text{int}})$ varies strongly in shape but is typically peaked which is challenging to capture using a G-based approach. In contrast, $P(j')$ varies least and can thus be predicted with the highest accuracy as can be seen from the lowest RMSD and R^2 values. The small difference in accuracy when comparing RMSD_{LG} and R_{LG}^2 to RMSD_{FG} and R_{FG}^2 arises because linear interpolation is used to obtain predicted amplitudes between the designated grid points.

Predictions of the STD model for three different sets of initial reactant states from the test set are shown in Figure 4. These data sets are characterized by 1) a R_{LG}^2 value closest to the average R_{LG}^2 value over the entire test set (77 sets) (panels A to C), and R_{LG}^2 values corresponding to 2) the largest (panels D to F; “best performing”) and 3) the smallest (panels G to I; “worst performing”) R_{LG}^2 values in the test set, respectively. The amplitudes of the product state distributions in panels D to F (lowest overall R_{LG}^2) are roughly one order of magnitude smaller compared to the other two data sets (panels A to F). This can be explained by the fact that the corresponding initial reactant state is characterized by $E_{\text{trans}} = 0.5$ eV, which results in a low reaction probability and renders a reactive collision a “rare” event. Consequently, the uncertainty arising from finite sample statistics in the QCT simulations is largest for such data sets. Moreover, 7 data sets with $E_{\text{trans}} = 0.5$ eV had already been excluded from the data set prior to training the NN because the reaction probability obtained from QCT was negligible. This naturally biases the NN training and predictions towards data sets with a larger reaction probability.

The product state distributions shown in Figure 4 demonstrate the variety of shapes and features that are present. This is a major difference compared to the product state distributions that were considered for the DTD models. There, only $P(v')$ was subject to significant variations, whereas $P(E'_{\text{trans}})$ and $P(j')$ showed less variability. Even for $P(v')$, three major classes of distributions could be distinguished which is not the case for STD. This variability explains the need for a denser grid and a more expressive NN in the present work.

Next, the performance of the STD model on a larger grid including parts of the training, test, validation set and additional initial (v, j) combinations is considered. For this, QCT simulations were carried out for $v \in [0, 15]$ with $\Delta v = 1$ and for $j = [0, 7, 15, 22, \dots, 157, 165]$.

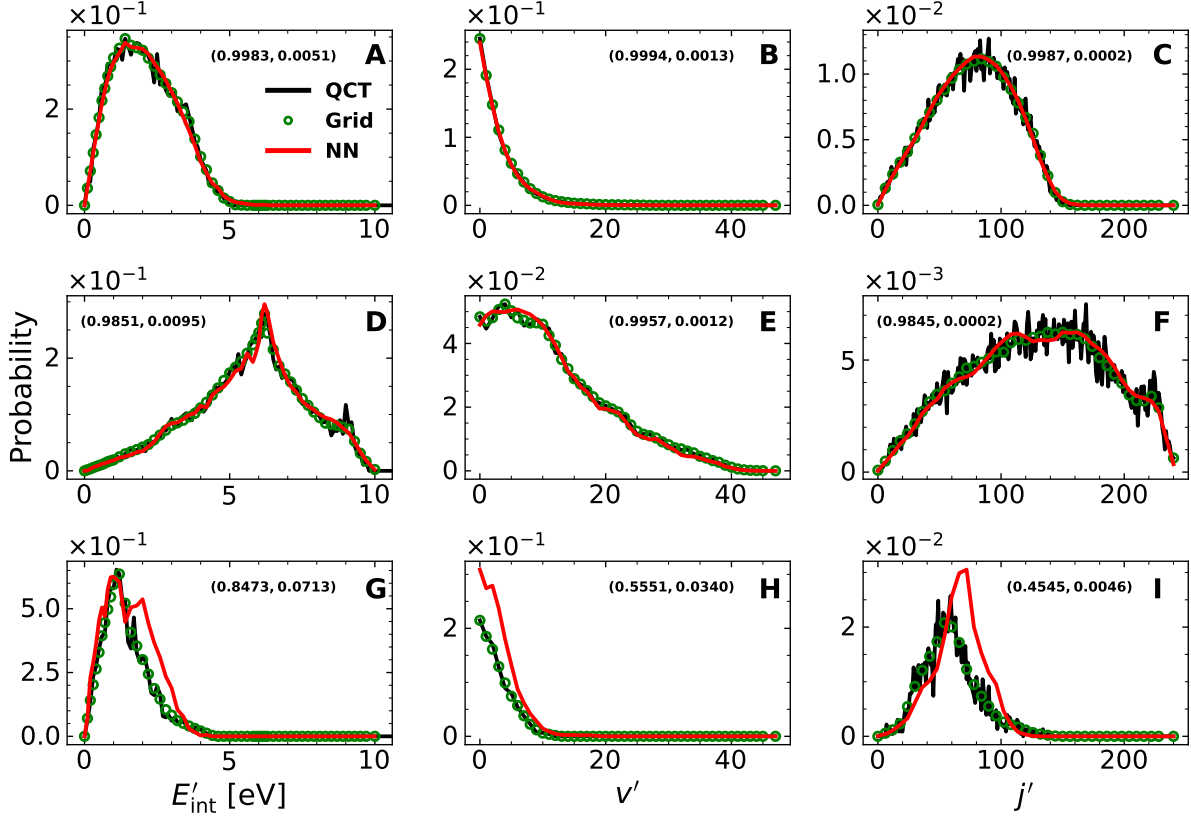


FIG. 4. Product state distributions obtained from explicit QCT simulations (QCT), and the corresponding reference amplitudes (Grid) and STD model predictions (NN) for three initial conditions from the test set (77 sets) not used in the training. The predictions for these three data sets are characterized by (A to C) a R^2_{LG} value closest to the mean R^2_{LG} value as evaluated over the entire test set, (D to F) the largest and (G to I) smallest R^2_{LG} value in the test set, respectively. (A to C) ($E_{\text{trans}} = 3.5$ eV, $v = 0$, $j = 45$, $E_{v,j} = 0.85$ eV), (D to F) ($E_{\text{trans}} = 6.0$ eV, $v = 21$, $j = 0$, $E_{v,j} = 1.11$ eV), (G to I) ($E_{\text{trans}} = 0.5$ eV, $v = 0$, $j = 135$, $E_{v,j} = 0.32$ eV). For each distribution ($R^2_{\text{LG}}, \text{RMSD}_{\text{LG}}$) values are provided.

The entire grid considered included 368 points and 50000 QCT simulations for every (v, j) combination were run at $E_{\text{trans}} = 4.0$ eV. Figure 5 reports the RMSD_{LG} between the product state distributions obtained from QCT and those predicted by the STD model. The two-dimensional surface $\text{RMSD}_{\text{LG}}(v, j)$ (for R^2_{LG} see Figure S2) exhibits a visible checkerboard pattern that reflects states (v, j) used for training (on-grid) and off-grid points which were not included in the training. Across the entire (v, j) state space the performance of STD is

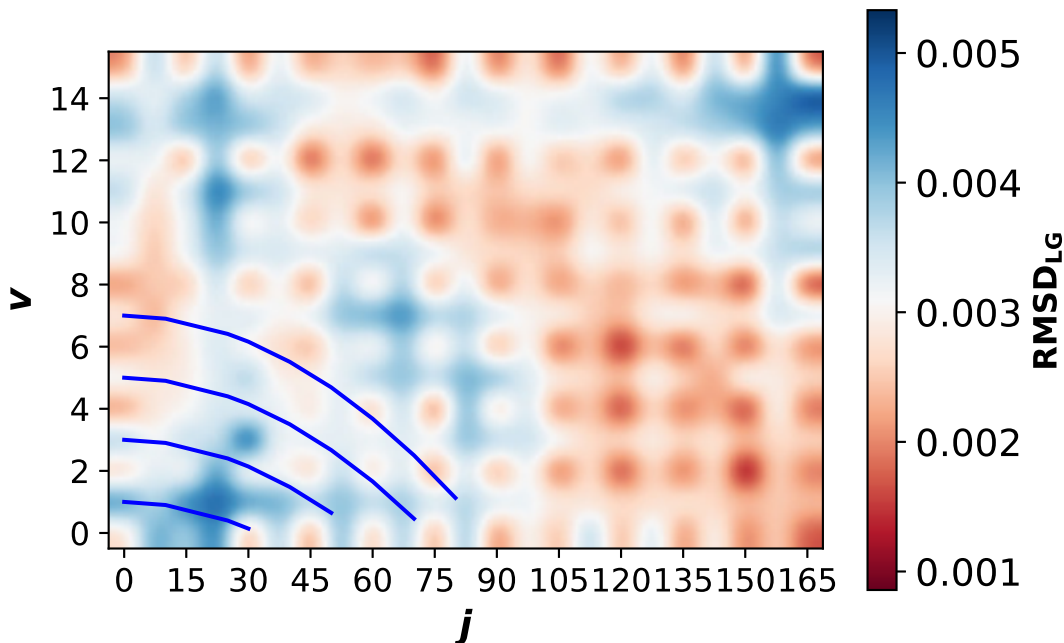


FIG. 5. 2D map for $\text{RMSD}_{\text{LG}}(v, j)$ between QCT and STD predictions for the product state distributions $P(E'_{\text{int}})$, $P(v')$, and $P(j')$ for given initial (v, j) . The STD model was evaluated at fixed $E_{\text{trans}} = 4.0$ eV for the grid points $v = [0, 2, \dots, 14]$ and $j = [0, 15, \dots, 165]$ used for training, validation, and test. For the off-grid points, the (v, j) -combinations included $v = [1, 3, \dots, 15]$ and $j = [7, 22, \dots, 157]$. The solid blue lines indicate constant rovibrational energies of 0.2850 eV, 0.6552 eV, 1.0142 eV, and 1.3622 eV. For the initial condition $(v = 13, j = 157)$ a comparatively high RMSD (~ 0.005) is obtained (blue). For the corresponding R_{LG}^2 map, see Figure S2.

good. Despite the low overall RMSD_{LG} , there are regions (blue) that are associated with larger differences between the reference QCT amplitudes and those from the STD model. For low (v, j) one reason for the somewhat larger RMSD_{LG} is the low reaction probability whereas for high (v, j) neglecting ro-vibrational coupling may lead to increased errors. A comparison of the final state distributions from QCT and the STD model for $(E_{\text{trans}} = 4.0$ eV, $v = 13, j = 157)$ and $(E_{\text{trans}} = 4.0$ eV, $v = 1, j = 22)$ is reported in Figures S3 and S4, respectively. A similar deterioration of performance in the high temperature regime was, for example, found from the surprisal model applied to the $\text{N}_2 + \text{N}$ reaction²⁵.

B. Performance for Initial Conditions from Reactant State Distributions

Next, the ability of the STD model to predict product state distributions given initial reactant state distributions is assessed. For this, the STD model is tested for different types of initial conditions by comparing reference product state distributions from explicit QCT simulations with those predicted by the model. For a given set of initial reactant state distributions initial conditions (E_{trans}, v, j) are generated through Monte Carlo sampling. In the limit of a sufficient number of samples, the average of the product state distributions predicted by the STD model will converge to the product state distributions associated with the given reactant state distributions. Sampling 10000 initial conditions is sufficient to converge the product state distributions obtained from STD (see Figure S5A). This compares with $\sim 10^6$ that are required for QCT simulations shown in Figure S5B. The decrease in the number of samples required for convergence is due to the more coarse-grained nature of the STD model compared to QCT as the STD model lacks state-to-state specificity for the products.

Four distinct cases of thermal distributions are considered in the following: $T_{\text{trans}} = T_{\text{vib}} = T_{\text{rot}}$, $T_{\text{trans}} \neq T_{\text{vib}} = T_{\text{rot}}$, $T_{\text{trans}} = T_{\text{vib}} \neq T_{\text{rot}}$, and $T_{\text{trans}} \neq T_{\text{vib}} \neq T_{\text{rot}}$. The performance measures of STD evaluated for the four cases are summarized in Table II. In all cases the STD model provides an accurate prediction of product state distributions given thermal reactant state distributions with $\text{RMSD}_{\text{FG}} \approx 0.003$ and $R_{\text{FG}}^2 \approx 0.996$. No significant differences in STD model performance for the different cases is observed which demonstrates that the STD model is generic in nature and applicable to reactant state distributions of arbitrary shape with significant weight over the range of initial reactant states considered in training. The decreased level of performance for predicting $P(E'_{\text{int}})$ distributions compared to $P(v')$ or $P(j')$ is again attributed to stronger variation in shapes and peaks near the NO dissociation as was already found for final state distributions from individual initial reactant states, see Table I. Moreover, the cutoff at $E_{\text{trans}} = 8.0$ eV in the training data of the STD model becomes relevant for $P(E'_{\text{int}})$ distributions at high temperatures and may lead to a decrease in performance.

For the most general case $T_{\text{trans}} \neq T_{\text{rot}} \neq T_{\text{vib}}$, 840 temperature combinations were generated.

| | RMSD _{FG} | | | | R_{FG}^2 | | | |
|--|--------------------|----------------------|---------|---------|------------|----------------------|---------|---------|
| | Overall | $P(E'_{\text{int}})$ | $P(v')$ | $P(j')$ | Overall | $P(E'_{\text{int}})$ | $P(v')$ | $P(j')$ |
| $T_{\text{trans}} = T_{\text{vib}} = T_{\text{rot}}$ | 0.0029 | 0.0079 | 0.0007 | 0.0001 | 0.9965 | 0.9912 | 0.9993 | 0.9990 |
| $T_{\text{trans}} \neq T_{\text{vib}} = T_{\text{rot}}$ | 0.0028 | 0.0078 | 0.0007 | 0.0001 | 0.9961 | 0.9904 | 0.9990 | 0.9990 |
| $T_{\text{trans}} = T_{\text{vib}} \neq T_{\text{rot}}$ | 0.0030 | 0.0083 | 0.0007 | 0.0001 | 0.9961 | 0.9900 | 0.9992 | 0.9990 |
| $T_{\text{trans}} \neq T_{\text{vib}} \neq T_{\text{rot}}$ | 0.0030 | 0.0081 | 0.0007 | 0.0001 | 0.9953 | 0.9885 | 0.9985 | 0.9989 |

TABLE II. Performance comparison of the STD model in terms of RMSD_{FG} and R_{FG}^2 for the 4 different temperature sets: $T_{\text{trans}} = T_{\text{vib}} = T_{\text{rot}}$ (61 sets), $T_{\text{trans}} \neq T_{\text{vib}} = T_{\text{rot}}$ (3637 sets), $T_{\text{trans}} = T_{\text{vib}} \neq T_{\text{rot}}$ (60 sets), and $T_{\text{trans}} \neq T_{\text{vib}} \neq T_{\text{rot}}$ (840 sets).

As Figure 6 demonstrates the STD model reliably captures overall shapes and features such as the position of maxima even for the worst performing data set (panels G to I). This is remarkable as the shapes of $P(E'_{\text{int}})$ and $P(v')$ can vary appreciably. The distribution of R^2 values for all 840 data sets also demonstrates high prediction accuracy, in particular for $P(v')$ and $P(j')$. The specific case $T_{\text{trans}} \neq T_{\text{vib}} = T_{\text{rot}}$ is considered in Figure S6. Panels S6A to C are for the best performing STD model compared with QCT data whereas panels D to F are representative for the average R_{FG}^2 . Both examples demonstrate that shapes and location of maxima are reliably captured by predictions based on the STD model. Even for the worst performing STD model (panels G to I) the important features of the distributions are still captured reliably. Finally, Figures S6J to L report the distribution $P(R_{FG}^2)$ for all 3637 models evaluated for $T_{\text{trans}} \neq T_{\text{vib}} = T_{\text{rot}}$. For all distributions $R_{FG}^2 > 0.95$ with $P(j')$ performing best.

A direct comparison of the STD and DTD models is reported in Table III. The two models perform on par for all measures and all degrees of freedom except for E'_{int} . This is despite the fact that the DTD model was explicitly trained on these thermal distributions (4658 data sets in total) and further underlines the predictive power of the STD model. Also, it should be noted that for the DTD model E'_{trans} instead of E'_{int} was used for training. Given the excellent performance of both models, the differences appear to be negligible. As such, STD represents a highly accurate approach to obtain product state distributions given initial state specific reaction states. The decreased level of performance for predict-

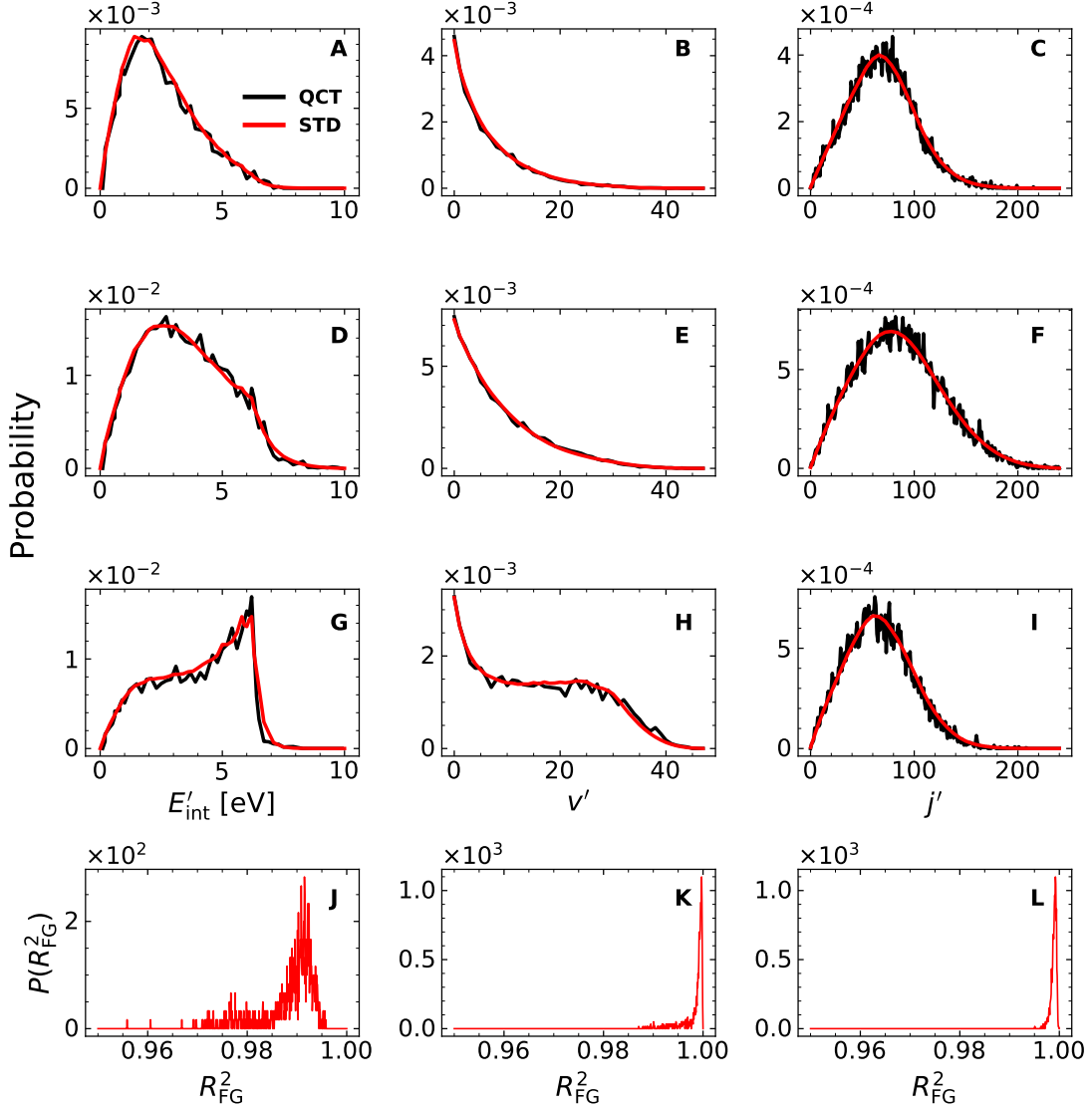


FIG. 6. Product state distributions for $T_{\text{trans}} \neq T_{\text{rot}} \neq T_{\text{vib}}$ obtained from STD and compared with explicit QCT simulations. Panels A-C: best performing prediction (largest R_{FG}^2) for $T_{\text{trans}} = 10000$ K, $T_{\text{vib}} = 6000$ K, $T_{\text{rot}} = 5000$ K; panels D-F: prediction closest to the mean R_{FG}^2 for $T_{\text{trans}} = 5000$ K, $T_{\text{vib}} = 8000$ K, $T_{\text{rot}} = 13000$ K; panels G-I: worst performing model (smallest R_{FG}^2) value for $T_{\text{trans}} = 5000$ K, $T_{\text{vib}} = 18000$ K, $T_{\text{rot}} = 8000$ K. Panels J-L: normalized distributions $P(R_{\text{FG}}^2)$ for the complete set of 840 temperatures ($T_{\text{trans}} \neq T_{\text{rot}} \neq T_{\text{vib}}$), respectively, (J) $P(E'_{\text{int}})$, (K) $P(v')$ and (L) $P(j')$.

ing $P(E'_{\text{int}})$ distributions compared to $P(v')$ or $P(j')$ (see RMSD_{FG} and R_{FG}^2) has several origins. First, $P(E'_{\text{int}})$ distributions vary strongly in shape and are typically peaked (see

Figure 2) which is challenging to capture using a G-based approach. Secondly, for highly excited (v', j') states rovibrational coupling in the diatomic product molecule becomes more important. Explicitly accounting for this coupling during the data preparation may further improve the predictive power of STD. In contrast to $P(E'_{\text{int}})$, rotational distributions $P(j')$ vary least and can thus be predicted with the highest accuracy. Moreover, the cutoff at $E_{\text{trans}} = 8.0$ eV in the training data of the STD becomes relevant for $P(E'_{\text{int}})$ distributions at high temperatures and may lead to a decrease in performance. The small decrease in accuracy when comparing RMSD_{LG} and R_{LG}^2 to RMSD_{FG} and R_{FG}^2 , see Table III, arises because of the linear interpolation to obtain predicted amplitudes between the designated grid points.

| | RMSD_{FG} | | R_{FG}^2 | |
|---------------|---------------------------|---------|-------------------|---------|
| | STD QCT | DTD QCT | STD QCT | DTD QCT |
| overall | 0.0030 | 0.0017 | 0.9953 | 0.9988 |
| E'_{α} | 0.0081 | 0.0042 | 0.9885 | 0.9985 |
| v' | 0.0007 | 0.0008 | 0.9985 | 0.9988 |
| j' | 0.0001 | 0.0001 | 0.9989 | 0.9991 |

TABLE III. Performance of STD and DTD models for $T_{\text{rot}} \neq T_{\text{vib}}$ (960 data sets) compared with QCT results for initial conditions from initial thermal distributions. For the STD model $\alpha = \text{int}$ and for DTD $\alpha = \text{trans}$. Performance measures (averaged over the all data sets) RMSD_{FG} and R_{FG}^2 are computed by comparing QCT data with the STD or DTD model predictions over the grid for which explicit QCT data is available. For $T_{\text{trans}} = 5000, 10000, 15000, 20000$ K a set of 960 temperatures is evaluated with $T_{\text{rot}} \neq T_{\text{vib}}$ ranging from 5000 to 20000 K with $\Delta T = 1000$ K.

It is also of interest to compare the performance of STD in predicting QCT data with the fidelity of the QCT data itself. As training of the NN is based on final state distributions from 8×10^4 trajectories for each initial condition it is likely that the training set does not contain fully converged reference information. To this end, a much larger number ($N_C = 5 \times 10^6$) of QCT simulations was carried out for a few initial conditions to determine the “ground truth” and were compared with final state distributions from only $N_U = 5 \times 10^4$ samples. The correlation for the bin-occupation between the “ground truth”, i.e. “converged” distributions from N_C samples, and the unconverged distributions using N_U

samples is $R^2 \sim 0.99$ or better for all four initial conditions considered and all three degrees of freedom, see Figure S7. Hence, the quality of the QCT reference data used for training the NN is comparable to the performance of the NN itself. The relative error between distributions from “ground truth” and the unconverged samples is around 0.2, see Figure S8. Thus, the χ^2 (rescaled mean squared error) between STD and reference QCT simulations accounting for the fact that the QCT input to train the NN is not fully converged is about 5 times larger than the RMSD, which yields $\chi^2 \sim 0.005$. One possible way of looking at this is to consider the amount of information (or signal) compared to the amount of noise. This “signal-to-noise ratio” should increase $\propto \sqrt{N}$ where N is the number of samples, assuming that the noise is stochastic and arising from insufficient sampling. As seen in Figure S8, when the number of samples in a channel is above ~ 10 , the noise/signal is 0.1.

The relevance of “rare events” is a major difference when considering product state distributions from individual initial reactant states compared to initial conditions from reactant state distributions. When applied to individual initial conditions it was found that the STD model performance decreases for $E_{\text{trans}} \leq 1.0$ eV, i.e. for initial conditions with low reaction probability. The corresponding product state distributions are noisy and show large variations due to finite sample statistics from QCT. This may be improved in future work through importance sampling of the impact parameter. While rare events are crucial for an accurate description of certain physical phenomena, such as plasma formation,²⁶ they do *not* constitute a significant contribution to product state distributions. As such, for observables that involve integration of a product state distribution, such as reaction rates, the decrease of performance of the STD model with regards to rare events is also negligible.

From the STD-predicted product state distributions, T -dependent reaction rates can be obtained and compared with rates from explicit QCT simulations. In general, such a rate is determined from

$$k(T) = g(T) \sqrt{\frac{8k_{\text{B}}T}{\pi\mu}} \pi b_{\text{max}}^2 P_{\text{r}}, \quad (5)$$

where P_{r} is the probability for a reaction to occur. For QCT simulations $P_{\text{r}} = \frac{N_{\text{r}}}{N_{\text{tot}}}$ where N_{r} is the number of reactive trajectories and N_{tot} is the total number of trajectories run. For the STD model, $P_{\text{r}} = \int_{E=0}^{E_{\text{max}}} P(E) dE$ where $E = E'_{\text{int}}$. For the forward $\text{N}(^4\text{S}) + \text{O}_2(\text{X}^3\Sigma_{\text{g}}^-)$

$\rightarrow \text{NO}(X^2\Pi) + \text{O}(^3\text{P})$ reaction on the $^4\text{A}'$ electronic state the degeneracy factor $g(T) = 1/3$ and μ is the reduced mass of the reactants.¹⁴ The two approaches are compared in Figure 7 and favourable agreement is found over a wide temperature range. Hence, the STD model can also be used to determine macroscopic quantities such as realistic reaction rates which is essential. The decrease in prediction accuracy at the highest temperatures may be attributed to the cutoff at $E_{\text{trans}} = 8.0$ eV in the training data of the STD. Cross sections $\sigma = \pi b_{\text{max}}^2 P_{\text{r}}$ were also determined for the test set ($N_{\text{test}} = 77$). Typical values for σ from the QCT simulations are $\sigma \sim 9 \times 10^{-15}$ cm² which compares with those from the STD model of $\sigma \sim 8.5 \times 10^{-15}$ cm².

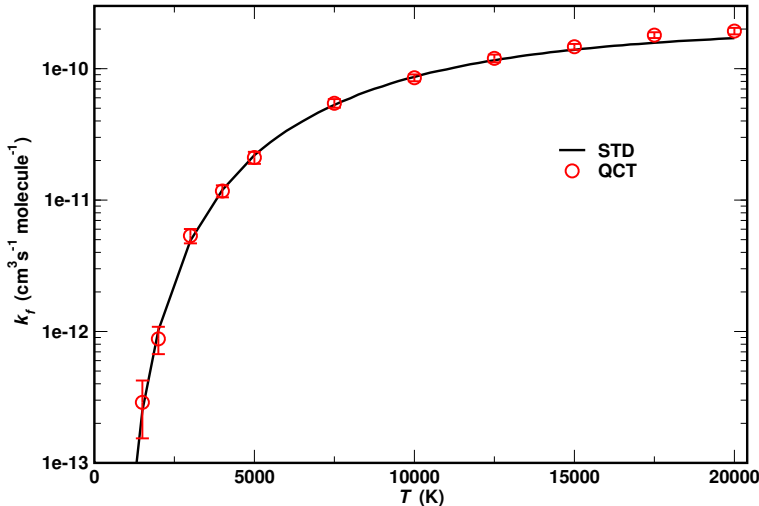


FIG. 7. The thermal forward rate k_f calculated from QCT (open red circle) and STD model (solid black line) for the $^4\text{A}'$ state of the $\text{N}(^4\text{S}) + \text{O}_2(X^3\Sigma_g^-) \rightarrow \text{NO}(X^2\Pi) + \text{O}(^3\text{P})$ reaction between 1500 and 20000 K. The present rates agree quantitatively with those directly obtained from QCT simulations.¹⁴ It is interesting to note that significant differences between the rates from QCT simulations and those from the STD model arise only for the highest temperatures for which pronounced $v - j$ coupling is expected.

Finally, it is also of interest to compare the computational cost for evaluating the STD and DTD models. Here, a single evaluation refers to the prediction of the product state distributions at 201, 48, and 241 evenly spaced points for E'_{int} (for STD) or E'_{trans} (for DTD) between 0 and 20 eV, $v' = 0 - 47$, and $j' = 0 - 240$, respectively, for a given reactant state distribution. The evaluation time for processing 50 reactant state distributions randomly

selected from the total set of 4658 distributions is (98.01 ± 5.95) s using the STD model and (1.03 ± 0.01) s using the DTD model on a 3.6 GHz Intel Core i7-9700K CPU. The difference of two orders of magnitude is explained as follows. For the STD model the NN is considerably larger and STD requires 10000 NN-evaluations for a given reactant state distribution. Contrary to that, for DTD only one evaluation is required. On the other hand, for STD linear interpolation is used to obtain an amplitude whereas DTD needs to evaluate a computationally costly kernel-based interpolation.

IV. DISCUSSION AND CONCLUSION

The present work introduces a machine-learned state-to-distribution model for predicting final state distributions from specific initial states of the reactants. The STD model achieves a good performance, see Tables I and III, and accurately predicts product state distributions as compared with reference QCT simulations. The model also allows to determine observables such as thermal reaction rates, see Figure 7.

One specific motivation to develop such an STD model is for generating meaningful input for direct simulation Monte Carlo²⁷ (DSMC) simulations. DSMC is a computational technique to simulate nonequilibrium high-speed flows and is primarily applied to dilute gas flows. The method is particle-based, where each particle typically represents a collection of real gas molecules, and transports mass, momentum, and energy. Models are required to perform collisions between particles by which they exchange momentum and energy with one another. For instance, given the internal energy states and relative translational energy of reactants in a colliding pair of particles, the total collision energy (TCE) model proposed by Bird is a widely used quantity to estimate the reaction probability²⁷. Once a colliding pair is selected for a collision, a key model output is the post-collision energy distribution from which product states are subsequently sampled. The state-of-the-art model for such a purpose is a phenomenological model proposed by Larsen-Borgnakke⁹ (LB). The explicit form of the

LB model for sampling the rotational and vibrational energy after a reaction is

$$f_{\text{LB}} = \frac{\left[1 - \frac{\varepsilon'_i}{\varepsilon_{\text{coll}}}\right]^{\zeta_{\text{tr}}/2-1}}{\sum_i \left[1 - \frac{\varepsilon'_i}{\varepsilon_{\text{coll}}}\right]^{\zeta_{\text{tr}}/2-1}}, \quad (6)$$

where ε'_i corresponds to ε'_v or ε'_j for post-reaction vibrational and rotational energy respectively and $\varepsilon_{\text{coll}} = \varepsilon'_v + \varepsilon'_j + \varepsilon'_t$. That is, the collision energy is the sum of the internal energy and translational energy post-collision (or pre-collision, due to conservation of total energy in the system the two coincide). In Eq. 6, $\zeta_{\text{tr}} = 5 - 2\omega$ is related to the translational degrees of freedom and the collision cross section parameter ω which is obtained by fitting collision cross sections such that the viscosity $\mu \propto T^\omega$ of a gas is recovered. In essence, the LB model is not based on state-specific probabilities of product states in reactions. Figure 8 reports the LB model results together with predictions from the STD model and reference QCT simulations. The significant discrepancies are not surprising as the LB model samples post-collision states from a local equilibrium distribution. This is the advantage of the STD model which is based on state-specific reference calculations from QCT simulations.

One additional refinement of the present method concerns preparation of the data set for training the NN. Including rotation/vibration coupling is likely to improve the overall model specifically for high (v, j) states. Furthermore, generating initial conditions from stratified sampling of the impact parameter may more broadly cover low-energy initial translational energies to further extend the range of applicability of the trained NN.

In conclusion, an initial state-resolved model to predict final state distributions for chemical reactions of type $A+BC \rightarrow AB+C$ based on machine learning is formulated and tested. The prediction quality of the model compared with explicit QCT simulations is characterized by $\text{RMSD} \sim 0.003$ and $R^2 \sim 0.99$. Final state distributions from STD can be sampled again using Monte Carlo simulations for generating input for more coarse grained simulations, such as DSMC. Furthermore, the STD model complements the DTD model when predicting product from reactant state distributions. At the cost of an increased evaluation time the STD model allows for accurate predictions given arbitrary nonequilibrium reactant state

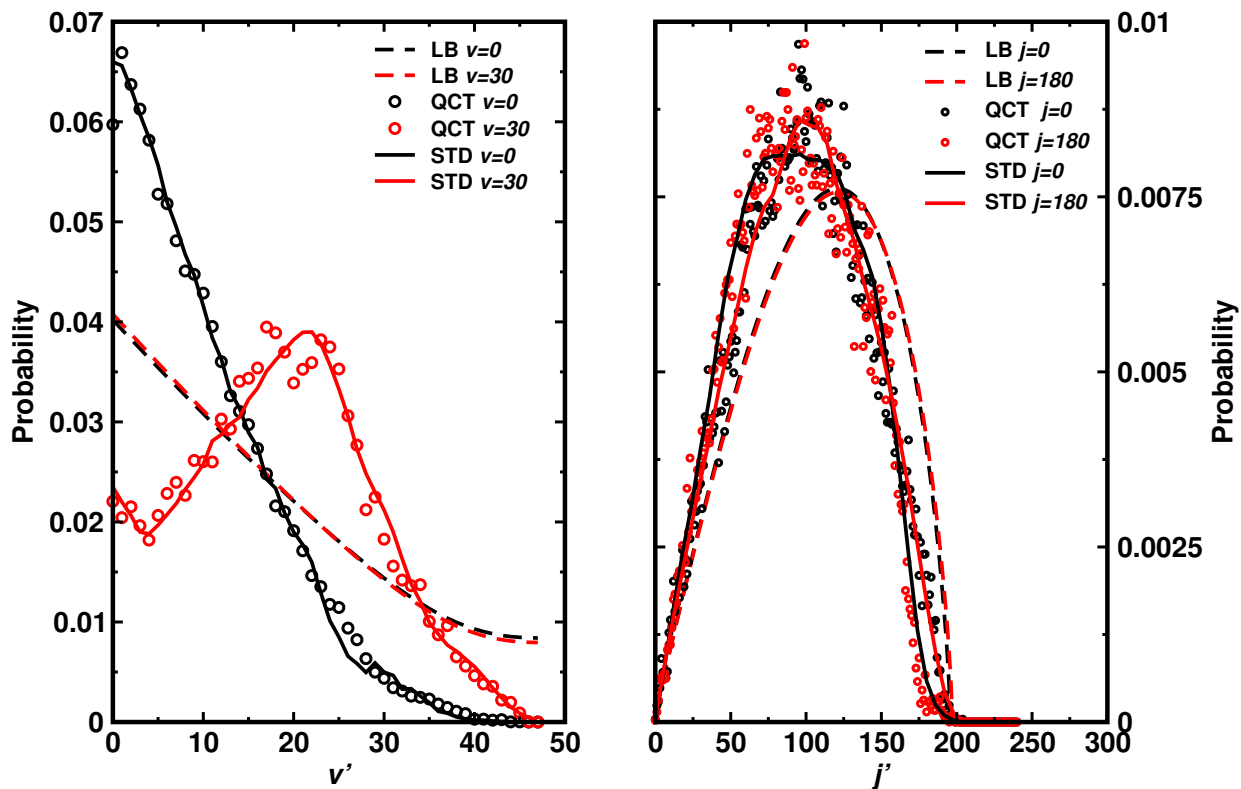


FIG. 8. Comparison of the final state distributions from the STD model and those from the Larsen-Borgnakke model which is often used in DSMC simulations. The initial conditions used are: $(E_{\text{trans}} = 7.0 \text{ eV}, v = 0, j = 0)$; $(E_{\text{trans}} = 2.5 \text{ eV}, v = 30, j = 0)$; $(E_{\text{trans}} = 2.0 \text{ eV}, v = 0, j = 180)$, all at the same $\varepsilon_{\text{coll}}$ or E_{tot} .

distributions. This is a regime for which DTD models trained on a given set of (equilibrium) reactant state distributions may underperform. In conjunction, these two models can enable the efficient and accurate simulation of molecular systems over time undergoing multiple reactive collisions.

DATA AND CODE AVAILABILITY

Exemplary data sets and code for evaluating STD models is available at <https://github.com/MMunibas/STD>.

SUPPORTING INFORMATION

The Supporting Information contains a detailed description of the local averaging procedure together with Figures S1-S8.

V. ACKNOWLEDGMENT

This work was supported by AFOSR, the Swiss National Science Foundation through grants 200021-117810, 200020-188724, the NCCR MUST, and the University of Basel.

REFERENCES

- ¹M. Meuwly, Chem. Res. **121**, 10218 (2021).
- ²M. S. Grover, E. Torres, and T. E. Schwartzentruber, Phys. Fluids **31** (2019).
- ³D. Koner, O. T. Unke, K. Boe, R. J. Bemish, and M. Meuwly, J. Chem. Phys. **150**, 211101 (2019).
- ⁴T. E. Schwartzentruber, M. S. Grover, and P. Valentini, Journal of Thermophysics and Heat Transfer **32**, 892 (2018).
- ⁵I. Goodfellow, Y. Bengio, and A. Courville, *Deep Learning* (MIT Press, 2016).
- ⁶J. Arnold, D. Koner, S. Käser, N. Singh, R. J. Bemish, and M. Meuwly, J. Phys. Chem. A **124**, 7177 (2020).
- ⁷I. D. Boyd and T. E. Schwartzentruber, *Nonequilibrium Gas Dynamics and Molecular Simulation* (Cambridge University Press, New York, 2017).
- ⁸D. Knight, J. Longo, D. Drikakis, D. Gaitonde, A. Lani, I. Nompelis, B. Reimann, and L. Walpot, Progr. Aerospace Sci. **48-49**, 8 (2012).
- ⁹C. Borgnakke and P. S. Larsen, J. Comput. Phys. **18**, 405 (1975).
- ¹⁰D. G. Truhlar and J. T. Muckerman, in *Atom - Molecule Collision Theory*, edited by R. B. Bernstein (Springer US, 1979) pp. 505–566.
- ¹¹N. E. Henriksen and F. Y. Hansen, *Theories of Molecular Reaction Dynamics* (Oxford, 2011).
- ¹²D. Koner, L. Barrios, T. González-Lezana, and A. N. Panda, J. Phys. Chem. A **120**, 4731 (2016).
- ¹³D. Koner, R. J. Bemish, and M. Meuwly, J. Chem. Phys. **149**, 094305 (2018).

- ¹⁴J. C. San Vicente Veliz, D. Koner, M. Schwilk, R. J. Bemish, and M. Meuwly, *Phys. Chem. Chem. Phys.* **22**, 3927 (2020).
- ¹⁵M. Karplus, R. N. Porter, and R. D. Sharma, *J. Chem. Phys.* **43**, 3259 (1965).
- ¹⁶J. D. Bender, P. Valentini, I. Nompelis, Y. Paukku, Z. Varga, D. G. Truhlar, T. Schwartzentruber, and G. V. Candler, *J. Chem. Phys.* **143**, 054304 (2015).
- ¹⁷Y.-R. Luo and J. Kerr, *CRC handb. chem. phys.* **89**, 89 (2012).
- ¹⁸K. He, X. Zhang, S. Ren, and J. Sun, in *Proceedings of the IEEE conference on computer vision and pattern recognition* (2016) pp. 770–778.
- ¹⁹C. Dugas, Y. Bengio, F. Bélisle, C. Nadeau, and R. Garcia, in *Advances in neural information processing systems* (2001) pp. 472–478.
- ²⁰D.-A. Clevert, T. Unterthiner, and S. Hochreiter, arXiv preprint arXiv:1511.07289 (2015).
- ²¹Y. A. LeCun, L. Bottou, G. B. Orr, and K.-R. Müller, in *Neural networks: Tricks of the trade* (Springer, 2012) pp. 9–48.
- ²²X. Glorot and Y. Bengio, in *Proceedings of the 13th International Conference on Artificial Intelligence and Statistics* (2010) pp. 249–256.
- ²³D. Kingma and J. Ba, arXiv preprint arXiv:1412.6980 (2014).
- ²⁴M. Abadi, A. Agarwal, P. Barham, E. Brevdo, Z. Chen, C. Citro, G. S. Corrado, A. Davis, J. Dean, M. Devin, *et al.*, arXiv preprint arXiv:1603.04467 (2016).
- ²⁵N. Singh and T. Schwartzentruber, *Proc. Natl. Acad. Sci.* **115**, 47 (2018).
- ²⁶A. Piel, *Plasma physics: an introduction to laboratory, space, and fusion plasmas* (Springer, 2017).
- ²⁷G. A. Bird, NASA STI/Recon Technical Report A **76** (1976).

Supporting Information: Machine Learning Product State Distributions from Initial Reactant States for a Reactive Atom-Diatom Collision System

S1. DETECTION OF “SHARP” PEAKS

When constructing the training, validation, and test data from the raw QCT data no local averaging was performed around "sharp" peaks and averaging over fewer points was done at nearby points. This was done to conserve the sharp peaks, as they would otherwise be washed out. A maximum of a given distribution was classified as “sharp” based on the following criteria:

For $P(E'_{\text{int}})$ if there were 2, 1, or 0 points to either side of the maximum, it was classified as sharp. Otherwise two linear fits were done to the 3 points (or 4 points, if available) to the left and right of a maximum, respectively, including the maximum itself. If the magnitude of both slopes exceeded a critical value $|a_{\text{crit}}| = 0.001$, the maximum was classified as “sharp”. Subsequently, averaging over neighbouring data points was performed: The maximum was not averaged, the nearest and next-nearest neighbours of the maxima were averaged with $n_{\text{max}} = 2$, and all other points were averaged with $n_{\text{max}} = 3$.

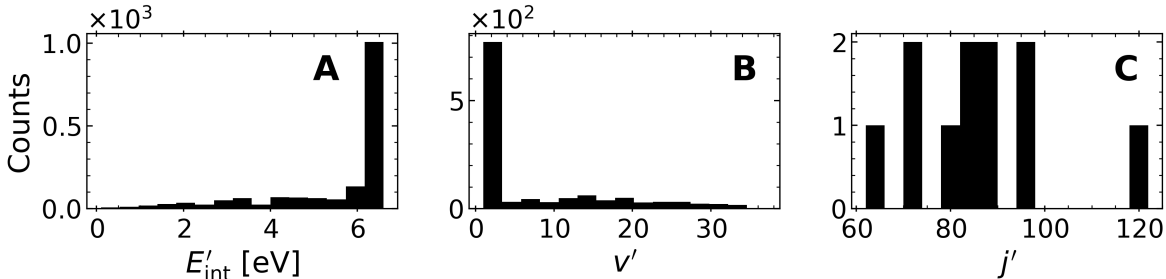


FIG. S1. Histograms showing the distribution of “sharp” peaks for (A) $P(E'_{\text{int}})$, (B) $P(v')$ and (C) $P(j')$ obtained by QCT simulations, considering all 2184 initial reactant states considered in the present work.

For $P(v')$ if there were 2, 1, or 0 points to either side of a maximum, it was classified as sharp. Otherwise two linear fits were performed for the 3 points to the left and right

of the maximum including the maximum itself. If the magnitude of both slopes exceeded a critical value $|a_{\text{crit}}| = 0.000143$, the maximum was classified as “sharp”. Subsequently, averaging over neighbouring data points was performed: The maximum was not averaged, and all other points were averaged with $n_{\text{max}} = 1$. The same procedure applied to $P(j')$ with $n_{\text{max}} = 7$ and $|a_{\text{crit}}| = 0.000005$. Figure S1 shows the distribution of “sharp” peaks for all 2184 explicit initial reactant states considered in this work.

S2. ADDITIONAL FIGURES

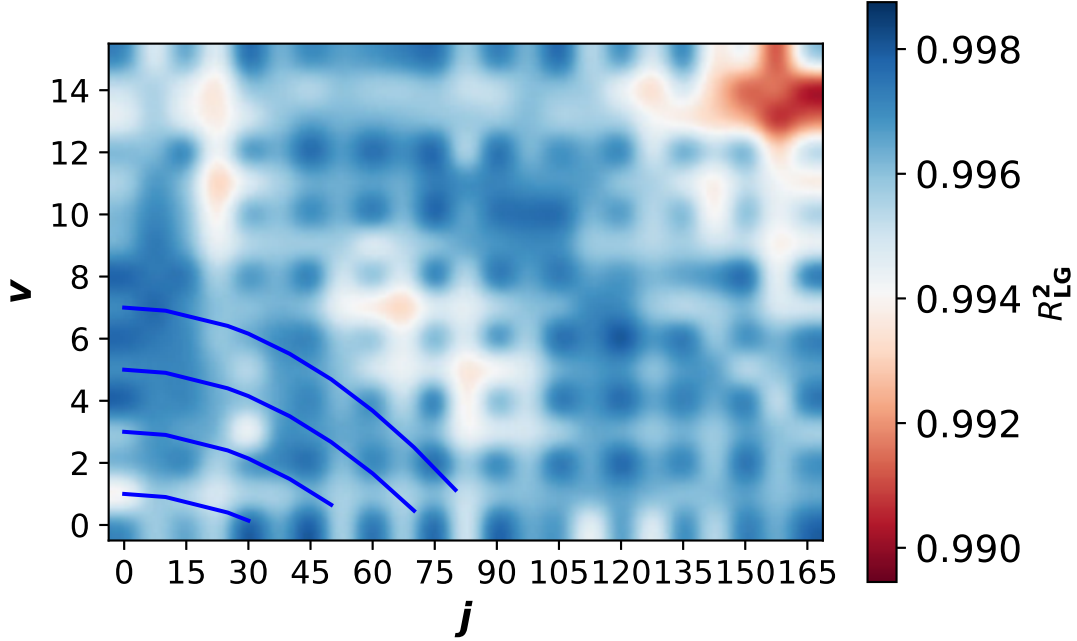


FIG. S2. 2D map of the R_{LG}^2 values between QCT and STD predictions for the product state distributions $P(E'_{\text{int}})$, $P(v')$, and $P(j')$ for given initial (v, j) . The STD model was evaluated at fixed $E_{\text{trans}} = 4.0$ eV for the grid points $v = [0, 2, 4, 6, 8, 10, 12, 14]$ and $j = [0, 15, 30, 45, 60, 75, 90, 105, 120, 135, 150, 165]$ used for training, validation, and testing. For the offgrid points, the (v, j) -combinations included $v = [1, 3, 5, 7, 9, 11, 13, 15]$ and $j = [7, 22, 37, 52, 67, 82, 97, 112, 127, 142, 157]$. The red lines are for constant rovibrational energies of 0.2850 eV, 0.6552 eV, 1.0142 eV, and 1.3622 eV. For the initial condition $(v = 13, j = 160)$ a low value of $R^2 = 0.94$ is obtained (red); the direct comparison between the final state distributions from QCT and those predicted from STD is given in Figure S3.

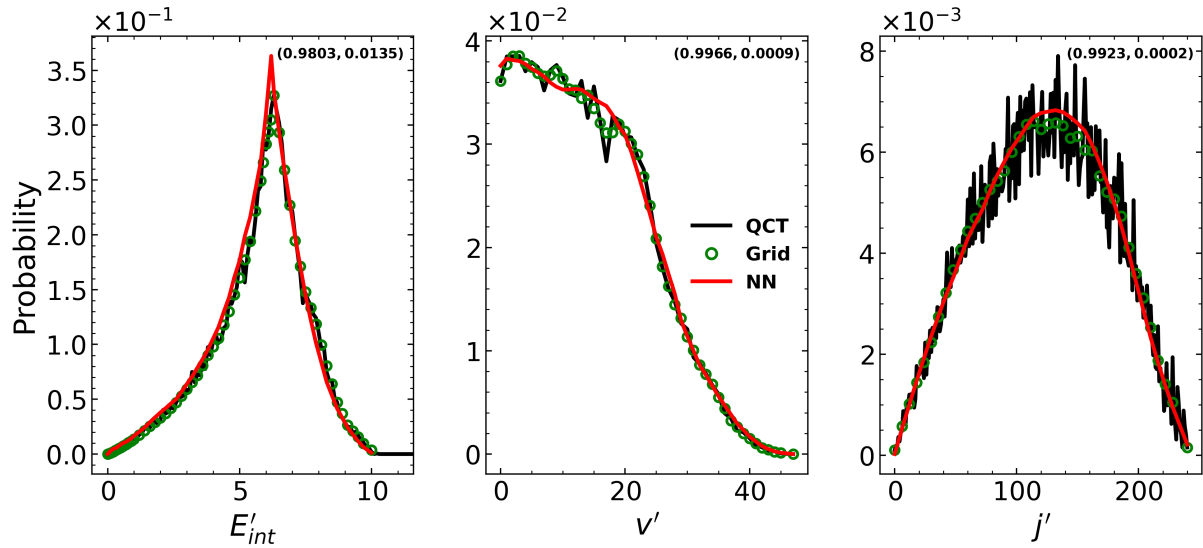


FIG. S3. Direct comparison between final state distributions from QCT simulations (black solid line) and those predicted from the STD model (red solid line) for ($E_{\text{trans}} = 4.0$ eV, $v = 13$, $j = 157$). The R_{LG}^2 and RMSD_{LG} for $P(E'_{\text{int}})$, $P(v')$ and $P(j')$ are shown in parenthesis. The overall R_{LG}^2 and RMSD_{LG} are 0.9897 and 0.0049, respectively.

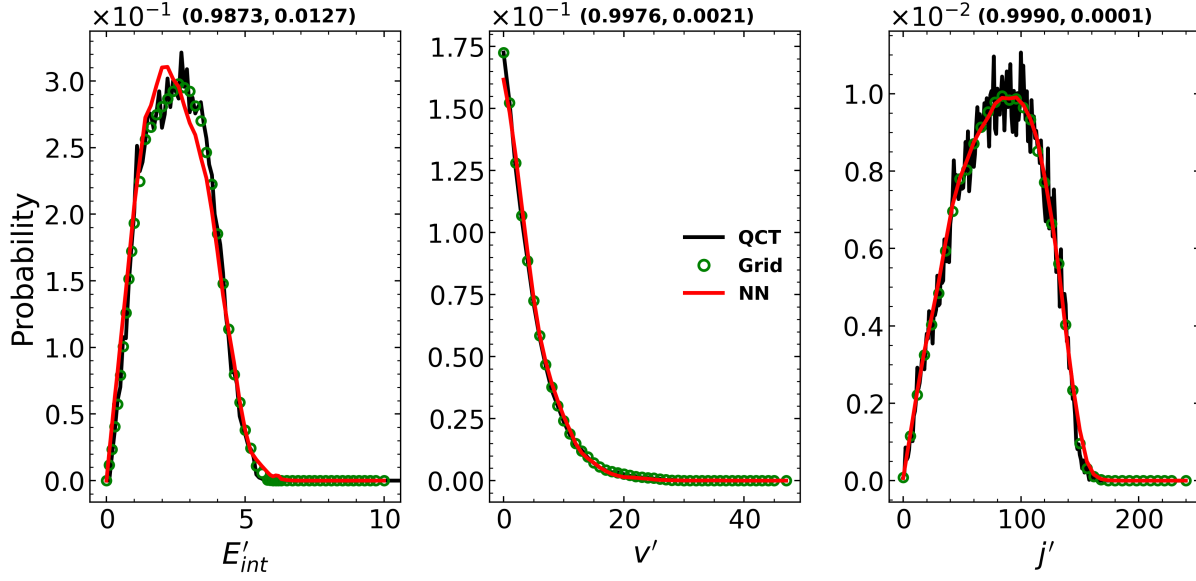


FIG. S4. Direct comparison between final state distributions from QCT simulations (black solid line) and those predicted from the STD model (red solid line) for initial condition ($E_{\text{trans}} = 4.0$ eV, $v = 1$, $j = 22$). The R_{LG}^2 and RMSD_{LG} for $P(E'_{\text{int}})$, $P(v')$ and $P(j')$ are shown in parenthesis. The overall R_{LG}^2 and RMSD_{LG} are 0.9946 and 0.0050, respectively.

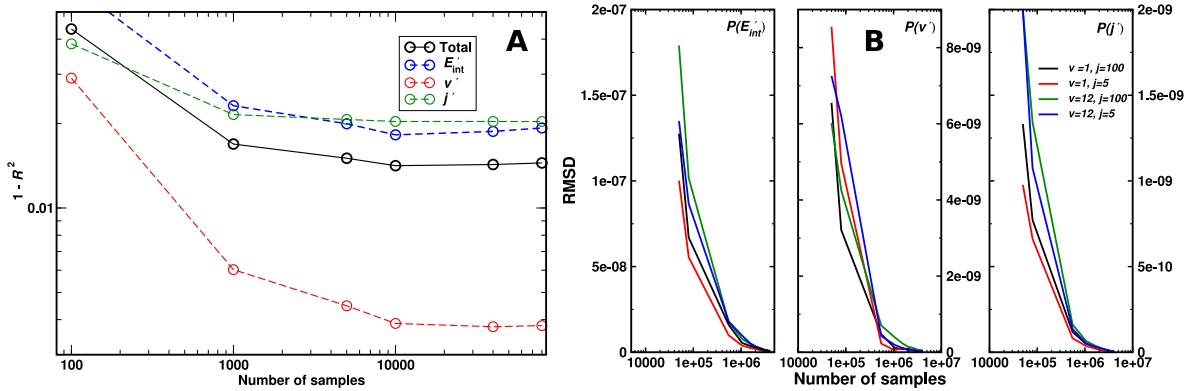


FIG. S5. Panel A: Error of the STD model in predicting product state distributions as a function of the number of samples drawn from the reactant state distributions. The error is reported as $1 - R_{\text{FG}}^2$, where R_{FG}^2 is obtained by averaging over the entire set of temperatures with $T_{\text{trans}} \neq T_{\text{vib}} \neq T_{\text{rot}}$. The error saturates at ≈ 10000 samples. Panel B: RMSD of QCT data as a function of different trajectories sample size with (5×10^6) trajectories as reference. Four different initial conditions ($v = 1, j = 100$; $v = 1, j = 5$; $v = 12, j = 100$; $v = 12, j = 5$) at $E_{\text{trans}} = 4.0$ eV are evaluated for $P(E'_{\text{int}})$, $P(v')$, and $P(j')$.

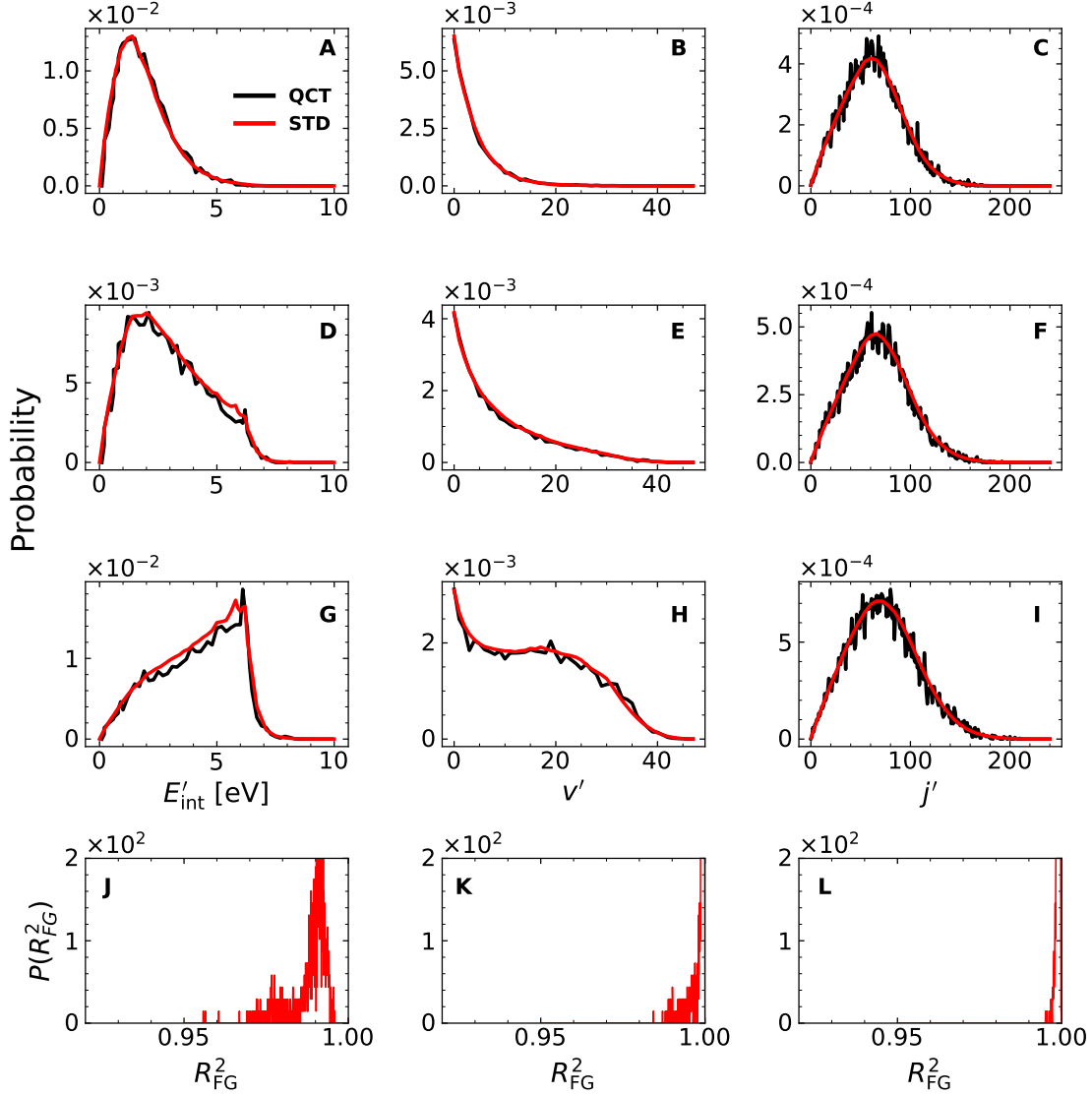


FIG. S6. Product state distributions for $T_{\text{trans}} \neq T_{\text{rot}} = T_{\text{vib}}$ from QCT simulations compared with predictions from the STD model for a set of temperatures between 5000 and 20000 K in steps of 250 K. For each set of temperatures 10000 reactant initial conditions are generated from Monte Carlo sampling of $(P(E_{\text{trans}}), P(v), P(j))$. Then, final state distributions $(P_i(E'_{\text{int}}), P_i(v'), P_i(j'))$ for each initial condition i are obtained from evaluating the STD model and averaged to obtain the final state distribution $(P(E'_{\text{int}}), P(v'), P(j'))$ for the particular set of temperatures. These distributions are then compared with the results from QCT simulations. Panels A-C: best performing (largest R_{FG}^2) for $T_{\text{trans}} = 6500$ K, $T_{\text{rot,vib}} = 5000$ K; panels D-F: closest to the mean of all models for $T_{\text{trans}} = 5250$ K, $T_{\text{rot,vib}} = 9250$ K; panels G-I: worst performing (smallest R_{FG}^2) for $T_{\text{trans}} = 5000$ K, $T_{\text{rot,vib}} = 19000$ K. Panels J to L report the distribution of R_{FG}^2 values for the complete set $T_{\text{trans}} \neq T_{\text{rot}} = T_{\text{vib}}$ containing for $P(E'_{\text{int}})$, (K) $P(v')$ and (L) $P(j')$, from left to right.

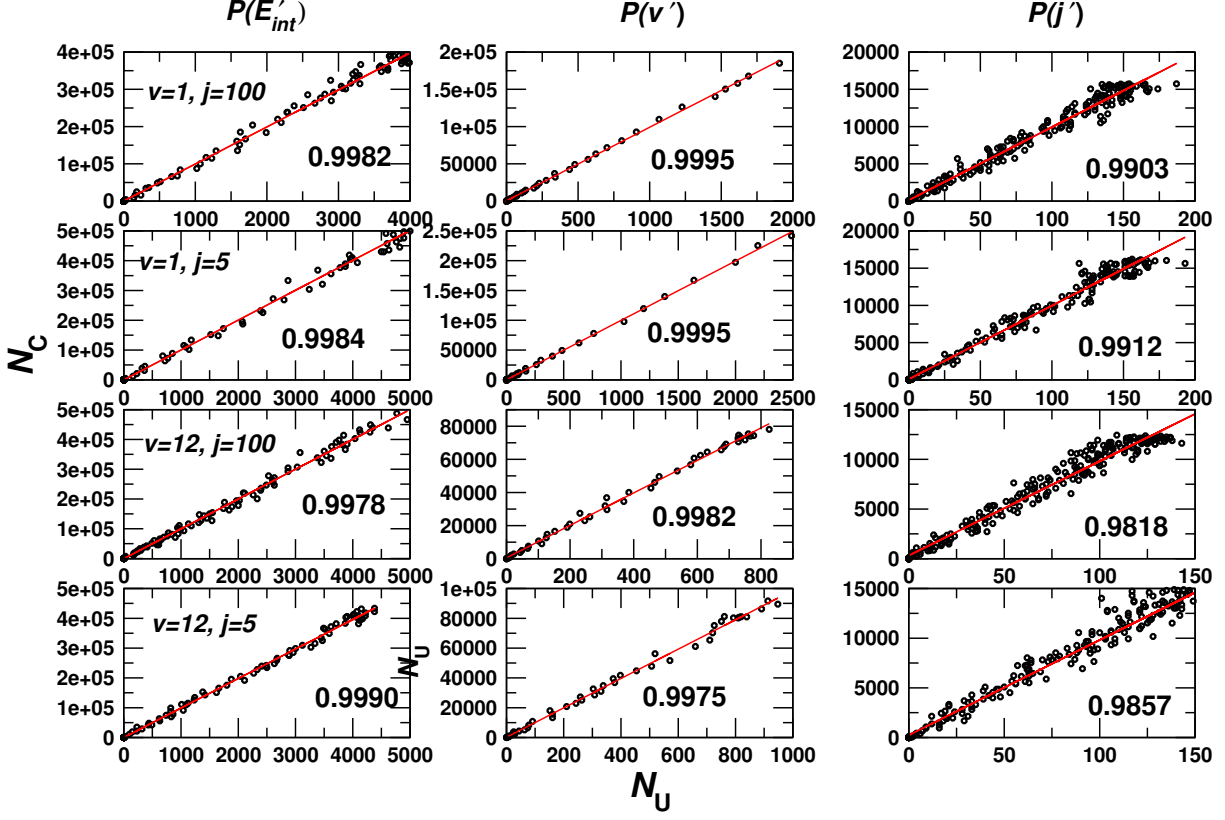


FIG. S7. Correlation between converged (“ground truth”, y -axis) and unconverged (x -axis) QCT simulations for four different initial conditions with $E_{\text{trans}} = 4.0$ eV as indicated. The “ground truth” is from 5×10^6 trajectories and the unconverged data is from 5×10^4 trajectories. The reported data compares occupation for the same bin for $P(E'_{\text{int}})$ (left), $P(v')$ (middle), and $P(j')$ (right). All correlation coefficients are close to 0.99 showing quantitative agreement.

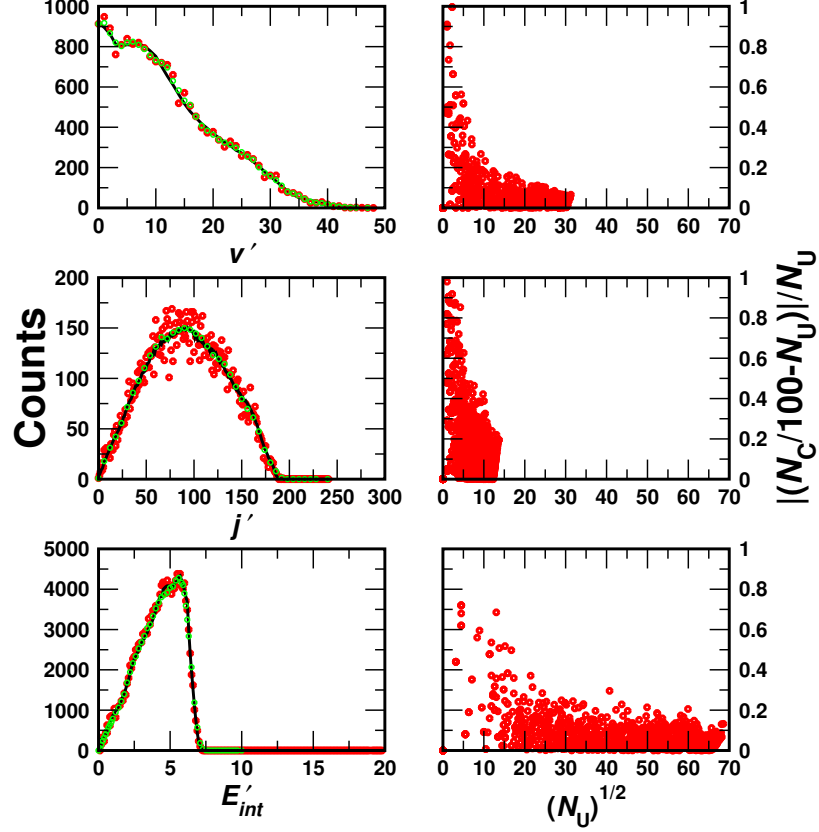


FIG. S8. Product state distributions $P(v')$, $P(j')$, and $P(E'_{\text{int}})$ for initial condition ($E_{\text{trans}} = 4.0$ eV, $v = 12, j = 5$), from $N_U = 5 \times 10^4$ (red, number of unconverged samples) and $N_C = 5 \times 10^6$ (black, “ground truth” number of converged samples) trajectories. The green dots are obtained by performing local averaging over the red data points. The reference curve obtained by local averaging of the unconverged QCT data matches the converged QCT data closely. This motivates the local averaging procedure performed as a data preparation step in this work. It allows for STD models to be trained on unconverged QCT data while the resulting models yield predictions that match the converged data closely. The right column reports the noise to signal ratio $\frac{(N_C/100 - N_U)/N_C}{N_C}$ of the unconverged set relative to “ground truth” as a function of $\sqrt{N_U}$.